electronics

MDPI

Article

Transient Stability Enhancement Strategy for Grid-Following Inverter Based on Improved Phase-Locked Loop and Energy Dissipation

Kezheng Jiang * and Dan Liu

Hubei Key Laboratory of Regional New Power Systems and Rural Energy System Configuration, Hubei Engineering Research Center of the Construction and Operation Control Technology of New Power Systems, State Grid Hubei Electric Power Research Institute, Wuhan 430077, China; dannyliu6@hotmail.com
* Correspondence: jiangkz21@163.com

Abstract

In a phase-locked loop (PLL) synchronized inverter grid-connected system, its equivalent damping coefficient is nonlinearly coupled with the operation power angle. Therefore, under a large disturbance, the indefinite damping increases the risk of transient instability in the system. To address this issue, firstly, a structurally modified IPLL is designed by removing the proportional coefficient branch of the traditional PLL and introducing a positive damping feedback branch. This design eliminates the coupling between the equivalent damping coefficient and the power angle, ensuring that the equivalent damping remains consistently positive. Secondly, based on the principle of energy dissipation via positive damping, a damping coefficient switching control strategy is developed. This strategy adaptively adjusts the damping during faults to rapidly dissipate excess kinetic energy, ensuring that the system returns to stability after fault clearance. Notably, the damping coefficient is pre-designed offline without relying on real-time grid parameters or operating data, enhancing the engineering practicability. Lastly, hardware-in-the-loop (HIL) experiments validate the strategy under extreme conditions.

Keywords: phase-locked loop; damping control; grid-following inverter; transient stability

check for updates

Academic Editor: Gianpaolo Vitale

Received: 29 July 2025
Revised: 27 August 2025
Accepted: 29 August 2025
Published: 3 September 2025

Citation: Jiang, K.; Liu, D. Transient Stability Enhancement Strategy for Grid-Following Inverter Based on Improved Phase-Locked Loop and Energy Dissipation. *Electronics* **2025**, *14*, 3520. https://doi.org/10.3390/electronics14173520

Copyright: © 2025 by the authors. Licensee MDPI, Basel, Switzerland. This article is an open access article distributed under the terms and conditions of the Creative Commons Attribution (CC BY) license (https://creativecommons.org/licenses/by/4.0/).

1. Introduction

With the increasing penetration of new energy in the power system, grid-following (GFL) inverters based on phase-locked loop (PLL) synchronization are widely used [1]. However, under some power system faults, the PLL may lose synchronization, which threatens the safety and stability of the power system. Thereby, the transient stability of grid-connected inverter systems has attracted widespread attention.

At present, one mechanism of transient instability in a grid-connected inverter system is the loss of stable equilibrium points. The major influence factors include the voltage drop degree, line impedance, and output current of the inverter [2]. However, even if the stable equilibrium point exists during the fault, the system is still faced with the risk of instability after cutting off the fault [3]. Phase portrait methods, energy function methods, and equal area criterion (EAC) are usually applied to quantitatively analyze the transient stability boundaries. The phase portrait is intuitive but cannot provide a stable region [4]. In [5], only considering the power angle range corresponding to the positive damping, Lyapunov's function is proposed to estimate the domain of attraction of the system's equilibrium point. However, due to the nonlinearity of the PLL dynamics, the damping of

the GFL inverter is defined [6,7], which leads to the domain of attraction calculated by [5] being conservative. Therefore, an improved Lyapunov function considering the effect of the defined damping is then designed to estimate the more accurate domain of attraction of the system's equilibrium point [8]. Additionally, the simplified two-order synchronization equation of the grid-connected GFL inverter system is also used to analyze the transient stability based on the EAC [9]. However, the traditional EAC supposes that the damping is always positive. The EAC-based analysis results may be inaccurate due to the indefinite damping of the GFL inverter. In [10,11], the modified EACs with varying damping are proposed. In summary, it can be seen that the indefinite damping of the GFL inverter caused by PLL dynamics brings many inconveniences to transient stability analysis and increases the risk of transient instability.

Studies have been performed to improve the transient stability under grid faults. The main methods improved include injection reactive current control, variable structure control, and damping enhancement control. In [12], S. Ma proposed that the ratio between the output active power and reactive power should be equal to the opposite number of impedance ratio of grid impedance to ensure the existence of equilibrium points during fault. However, it relies on an accurate estimation of grid impedance. In [13], a voltage-dependent active and reactive current injection during fault ride-through is proposed to enhance transient stability. As for variable structure and damping enhancement control, these are, in general, used simultaneously. In [14,15], the adaptive PI parameters of PLL are used based on fault information to enhance the damping under fault. In [16], a voltage normalization control is proposed to increase the damping ratio of PLL. Further, in [17], the impacts of filter delay in PLL on the transient stability of grid-following inverters are revealed, and a novel filter is proposed. In [18], through the improved q-axis current control of GFL, the transient voltage stability is enhanced, thereby improving transient synchronous stability. However, the above methods are still based on the traditional PLL structure, and the nonlinearity coupling between the power angle and PI parameters is not overcome. Therefore, no matter how the PI parameters of PLL are selected, the equivalent damping coefficient of the system quickly varies with the change in operation power angle during the faults, which causes the indefinite damping characteristic and increases the risk of transient instability in the traditional PLL-synchronized inverter grid-connected system. Furthermore, ref. [19] freezes the PLL during the fault, but the output currents lose control. In [20], only the integrator in PLL's PI controller is frozen during faults, which guarantees that the inverter has infinite damping as a first-order system. However, the first-order PLL cannot eliminate the static error under the varying grid frequency. In order to clarify the advantages and disadvantages among different methods, comparisons are listed in Table 1.

Table 1. Comparisons among different methods for enhancing transient stability of grid-following inverter.

Methods	Global Transient Stability	Estimation of Grid Impedance	Indefinite Damping	Tracking Performance Under the Varying Grid Frequency	Advantages	Limitations
Adaptive power/current control [12,13,18]	No	Need	Yes	Good	These methods are easily applied without changing PLL's structure	Information about grid impedance is needed and cannot eliminate the indefinite damping
Optimization of PLL's PI parameters [14–17]	No	None	Yes	Good		Cannot eliminate the indefinite damping

Table 1. *Cont.*

Methods	Global Transient Stability	Estimation of Grid Impedance	Indefinite Damping	Tracking Performance Under the Varying Grid Frequency	Advantages	Limitations
Freezing the PLL [18,19]	Yes	None	None	Static error	Eliminate the indefinite damping and keep global transient stability	Cannot eliminate the static error under the varying grid frequency
Proposed method	Yes	None	None	Good	Eliminate the indefinite damping and keep global transient stability	None

In short, the traditional PI-type PLL cannot eliminate the indefinite damping characteristic because of the nonlinearity coupling between the power angle and PI parameters. The parameter freezing of the traditional PI-type PLL damages tracking performance. Therefore, solving the indefinite damping in the traditional PLL and designing a reasonable damping to guarantee the transient stability of inverter are still necessary and have not yet been achieved.

To fill this gap, a transient stability enhancement strategy for grid-following inverters based on the improved PLL and energy dissipation is proposed in this paper. The main contributions of this paper are summarized as follows.

(1) An improved PLL is proposed to eliminate the coupling between the equivalent damping coefficient and the power angle, and then the positive equivalent damping coefficient is always guaranteed. As a result, the problem of indefinite damping in traditional PLL is overcome.
(2) Based on the principle of utilizing positive damping to dissipate energy in an improved PLL, a switching control strategy of the damping feedback coefficient is proposed to ensure the transient stability of the system under large disturbances.
(3) The damping coefficient is an offline design that does not need to use grid parameter information or system operation parameter data.

This paper is organized as follows: Section 2 describes the model of the improved PLL-synchronized inverter. In Section 3, the stability regions of traditional PLL-synchronized inverter and improved PLL-synchronized inverter are compared. In Section 4, a damping design method for guaranteeing transient stability is proposed. Experimental verifications are presented in Section 5. Finally, conclusions are drawn in Section 6.

2. Modeling of Inverter Grid-Connected System

2.1. Modeling of the Traditional PLL-Synchronized Inverter

The circuit and control structure of a traditional PLL-synchronized inverter is shown in Figure 1. In Figure 1, V_{abc} and V_g represent the PCC voltage and grid voltage. I_{abc} is the current injected into the grid. The grid impedance is represented by Z_g. Vdc is the DC voltage, which is assumed to be constant. Additionally, since the dynamic of the current loop is faster than PLL, the impacts of the current loop in analyzing the transient stability are not considered. Moreover, in a PLL-synchronized inverter, the virtual power angle δ is

defined as the difference between the phase angle of PCC's voltage and the phase angle of grid voltage. As a result, the simplified model of a PLL-synchronized inverter connected to the grid is shown in Figure 2.

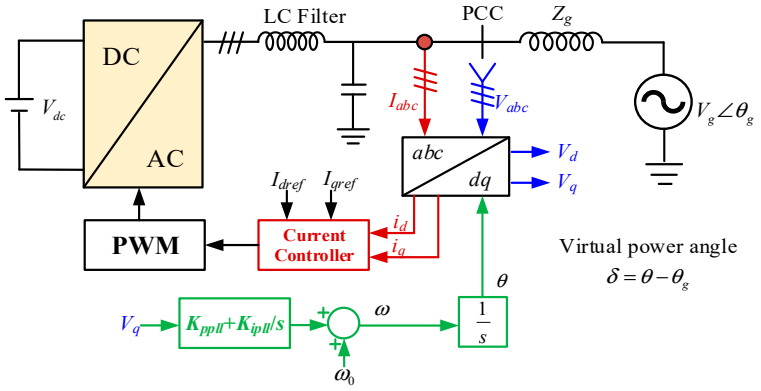


Figure 1. Circuit and control structure of a traditional PLL-synchronized inverter.

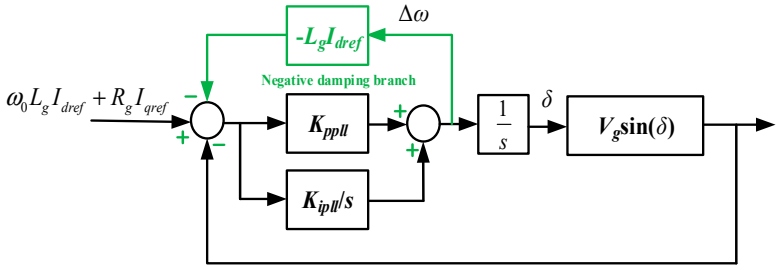


Figure 2. Transfer function block diagram of a traditional PLL-synchronized inverter.

According to Figure 2, the second-order synchronization equation of a traditional PLL-synchronized inverter is shown in Formula (1):

$$\begin{cases} \dot{\delta} = \omega - \omega_0 \\ \underbrace{\frac{1 - K_{ppll}L_gI_{dref}}{K_{ipll}}}_{J_{eq}}\ddot{\delta} = \underbrace{\omega_0 L_g I_{dref} + R_g I_{qref}}_{P_m} - \underbrace{V_g \sin\delta}_{P_e} \\ - \underbrace{\left[\underbrace{\frac{K_{ppll}V_g}{K_{ipll}}\cos\delta}_{D_{eq1}} \underbrace{-L_gI_{dref}}_{D_{eq2}}\right]}_{D_{eq}}(\omega - \omega_0) \end{cases} \quad (1)$$

In Formula (1), P_m represents the equivalent mechanical power, P_e represents the equivalent electromagnetic power, J_{eq} represents the equivalent inertia coefficient, and D_{eq} represents the equivalent damping coefficient. From Formula (1), it can be seen that both equivalent inertia and damping coefficients vary under different grid impedance and operation currents. With increasing grid impedance and operation current, the equivalent inertia coefficient is decreased. Also, the equivalent damping coefficient of a traditional PLL-synchronized inverter is indefinite. Under the inverter mode, D_{eq2} is always negative. Since the power angle is generally in $(-\pi/2, \pi/2)$, D_{eq1} is nonnegative. However, under the weak-grid condition and high-power operation mode, the operation power angle is close to $\pi/2$, and cos δ is also close to zero. Therefore, no matter how the PI parameters

of PLL are selected, the positive damping component will quickly deteriorate under ultra-weak-grid conditions. Additionally, if the system has no equilibrium point during faults, the equivalent damping coefficient will exhibit positive and negative alteration due to the periodicity of the trigonometric function, which is not conducive to transient stability [7].

2.2. Modeling of the Improved PLL-Synchronized Inverter

According to the previous analysis results, the strong coupling between the proportional parameter in PLL and the operation power angle is the main reason for the indefinite equivalent damping coefficient. Therefore, the proportional loop in PLL is removed and a positive damping feedback branch is added. The structure of an improved PLL (IPLL) is shown in Figure 3.

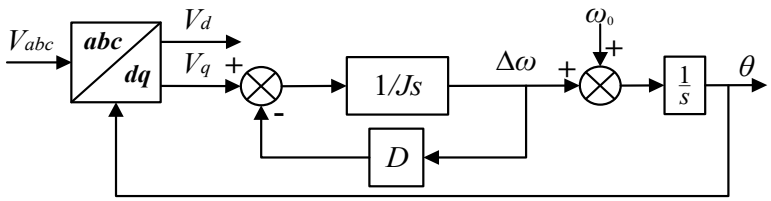


Figure 3. Control structure of an improved PLL.

However, the proposed structure in Figure 3 cannot catch the real phase of PCC voltage under grid frequency variation. Therefore, a practical IPLL requires a phase compensation branch in a steady state. The q-axis voltage can be written as follows:

$$V_q = D(\omega - \omega_0) \tag{2}$$

If the real grid frequency is not equal to the reference grid frequency, the steady state of the q-axis voltage is not equal to zero. The phase error between the locked phase by IPLL and the real phase can be expressed as

$$\varphi_0 = \arcsin\frac{V_{q0}}{V_0} = \arcsin\frac{D}{V_0}\Delta\omega \tag{3}$$

Considering the compensation branch is only worked in a steady state, an output limit is set to avoid the impacts of the transient shock in the measured grid frequency. Therefore, the practical IPLL is as shown in Figure 4.

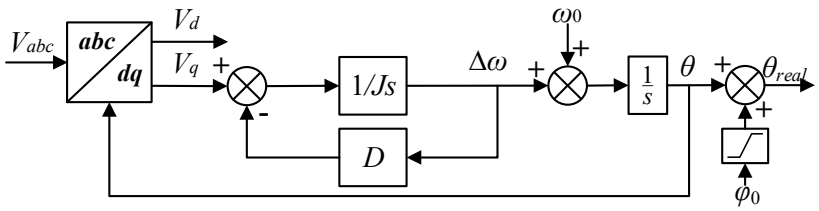


Figure 4. Practical control structure of an IPLL.

In Figure 4, the output phase θ is used to achieve the Park transformation of voltage, and the phase θ_{real} is used to achieve the Park transformation of current. When the grid frequency is the same as the reference frequency, the phase θ_{real} is equal to θ.

According to Figure 1, the PCC's voltage is expressed in the dq-frame as

$$\mathbf{V}e^{j(\theta_V-\theta)} = \mathbf{I}e^{j(\theta_I-\theta)}\mathbf{Z}_g + V_g e^{j(\theta_g-\theta)} \tag{4}$$

From Formula (4), the q-axis voltage can be expressed:

$$V_q = -V_g \sin\delta + \omega L_g I_d + R_g I_q \tag{5}$$

In Formula (5), since the current loop is faster than the PLL, the real *dq* currents are equal to current references. Therefore, the transfer function block diagram of an IPLL-synchronized inverter is as shown in Figure 5.

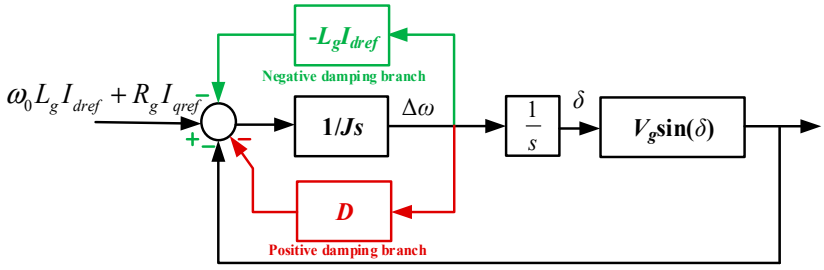


Figure 5. Transfer function block diagram of an IPLL-synchronized inverter.

According to Figure 5, the second-order synchronization equation of an IPLL-synchronized inverter is written in Formula (6). It can be found that the equivalent damping coefficient is decoupled with the power angle. The equivalent damping coefficient D_{eq} can always be positive while selecting a suitable feedback gain D.

$$\begin{cases} \dot{\delta} = \omega - \omega_0 \\ \underbrace{J}_{J_{eq}}\ddot{\delta} = \underbrace{\omega_0 L_g I_{dref} + R_g I_{qref}}_{P_m} - \underbrace{V_g \sin\delta}_{P_e} - \underbrace{\left[D - L_g I_{dref}\right]}_{D_{eq}}(\omega - \omega_0) \end{cases} \tag{6}$$

3. Stability Regions of PLL-Synchronized Inverters

3.1. Construction of Energy Function

According to Formulas (1) and (6), space equations of traditional PLL- and IPLL-synchronized inverters are similar to the rotor motion equation of synchronous generators, and can be written in a general form, as shown in Formula (7):

$$J_{eq}\ddot{\delta} = P_m - P_e - D_{eq}\dot{\delta} \tag{7}$$

The first integration method is used to construct a suitable energy function [21]. As a result, the energy function can be presented as follows:

$$V\left(\delta, \dot{\delta}\right) = -P_m\delta - V_g\cos\delta + \frac{1}{2}J_{eq}\dot{\delta}^2 + E_0 \tag{8}$$

From Formula (8), the equivalent kinetic energy E_K and the equivalent potential energy E_P of the system are as expressed in Formulas (9) and (10)

$$E_K = \frac{1}{2}J_{eq}\dot{\delta}^2 \tag{9}$$

$$E_P = -P_m\delta - V_g\cos\delta + E_0 \tag{10}$$

where E_0 is a constant to ensure energy function $V > 0$.

According to Formulas (7) and (8), the derivative of Formula (8) is expressed in Formula (11):

$$\dot{V}(\delta, \dot{\delta}) = J_{eq}\ddot{\delta}\dot{\delta} - P_m\dot{\delta} - V_g \sin\delta\dot{\delta} = -D_{eq}\dot{\delta}^2 \tag{11}$$

From Formula (11), it can be seen that the proposed energy function in Formula (8) is effective only in the range that has a positive equivalent damping coefficient.

3.2. Comparison of Stability Region Between PLL-Synchronized Inverter and IPLL-Synchronized Inverter

The theory of Russell invariant sets can be used to obtain the conservative stable regions of different synchronized inverters [8,22]. According to Formula (1), the equivalent damping coefficient in a traditional PLL-synchronized inverter is affected by power angle. The maximum power angle of the system at $D_{eq} = 0$ is expressed as follows:

$$\delta_{PLL\max} = \arccos\frac{K_{ipll} I_{dref} L_g}{K_{ppll} V_g} \tag{12}$$

Therefore, the energy at $\delta_{PLL\max}$ can be regarded as the maximum critical energy after faults.

As for the IPLL-synchronized inverter, since its equivalent damping coefficient can be always positive, the energy at the unstable equilibrium point (UEP) can be regarded as the maximum critical energy after faults. The UEP is expressed as follows:

$$\delta_{IPLL\max} = \pi - \arcsin\frac{\omega_g L_g I_{dref} + R_g I_{qref}}{V_g} \tag{13}$$

According to Formulas (12) and (13), it can be seen that the maximum critical energies after faults in two different synchronized inverters are related to the operation and control parameters. To fairly compare the PLL-synchronized and IPLL-synchronized inverters, their equivalent damping and inertia coefficients are set as the same values under the same operation power angle δ_s. The relationships between parameters in PLL and IPLL are expressed as follows:

$$K_{ppll} = \frac{DK_{ipll}}{V_g \cos\delta_s}, K_{ipll} = \frac{JV_g \cos\delta_s}{V_g \cos\delta_s + JDL_g I_{dref}} \tag{14}$$

According to Table 1, under the conditions of L_g = 4.1 mH (SCR = 3), the parameters of the IPLL-synchronized inverter are set as D = 2, J = 0.05. Therefore, according to Formula (11), the PI parameters of the PLL-synchronized inverter are set as K_{ppll} = 0.13 and K_{ipll} = 19.144. Under this condition, the step responses are tested by electromagnetic transient models. The simulation results shown in Figure 6 indicate that two synchronized inverters have similar dynamic performance if they have the same equivalent damping coefficient and inertia coefficient. Under this specific case, according to Formulas (8), (12) and (13), the stable regions of traditional PLL- and IPLL-synchronized inverters are as shown in Figure 7. The system will converge to the equilibrium point from any initial state within the stable region. This confirms that positive damping guarantees the system's asymptotic stability in the Lyapunov sense [23,24].

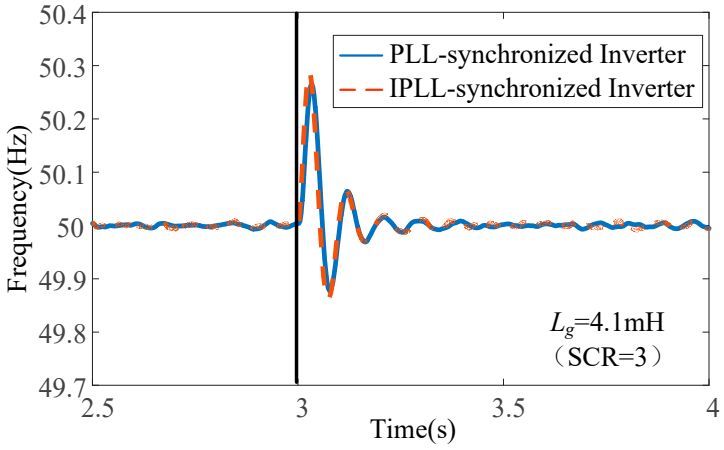


Figure 6. Simulation results under Lg = 4.1 mH (SCR = 3).

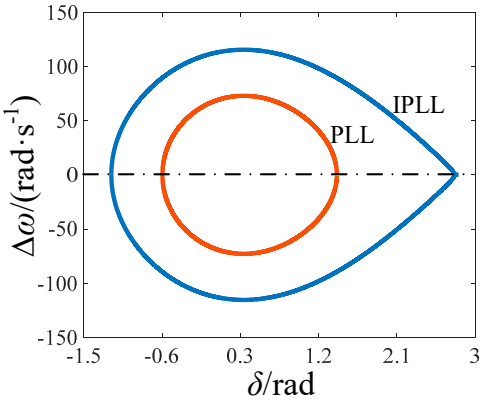


Figure 7. Stable regions of traditional PLL- and IPLL-synchronized inverters.

4. Transient Stability Enhancement Control of IPLL-Synchronized Inverter

4.1. Parameter Design of IPLL

In traditional power systems, the transient stability of power angle refers to the system's ability to maintain stability during the first or second swing of the synchronous machine after fault clearance. If the system has sufficient damping to dissipate the increased kinetic energy during the transient process, the power angle will eventually stabilize at the stable equilibrium point of the cycle at the moment that the fault is cleared. In fact, the power angle curve of the system has an equilibrium point in each cycle. If the kinetic energy of the system is completely consumed by the damping of multiple periods, the power angle is finally restored to the stable equilibrium point of the subsequent period. Therefore, the transient stability constraint of IPLL damping design is derived from the perspective of fault recovery.

Considering the effect of damping, Formula (15) can be obtained by multiplying both sides of Formula (7) by dδ/dt:

$$J_{eq}\ddot{\delta}\frac{\mathrm{d}\delta}{\mathrm{d}t} = P_m\frac{\mathrm{d}\delta}{\mathrm{d}t} - P_e\frac{\mathrm{d}\delta}{\mathrm{d}t} - D_{eq}\dot{\delta}\frac{\mathrm{d}\delta}{\mathrm{d}t} \tag{15}$$

Formula (16) can be obtained by integrating and sorting Formula (15):

$$\frac{1}{2}J_{eq}\dot{\delta}^2 = -\left(-P_m\delta - V_g\cos\delta + E_0\right) - D_{eq}\int\dot{\delta}\mathrm{d}\delta \tag{16}$$

From Formula (16), the energy consumed by damping can be expressed as

$$E_D = D_{eq} \int \dot{\delta} \mathrm{d}\delta \tag{17}$$

Combined with the above analysis, the energy conversion relationship of the system is expressed as follows:

$$E_K + E_P + E_D = 0 \tag{18}$$

The energy consumed by damping and the variation in potential energy in the process of the power angle of the system from δ_a to δ_b is expressed as Formulas (19) and (20), respectively.

$$E_D = D_{eq} \int_{\delta_a}^{\delta_b} \dot{\delta} \mathrm{d}\delta \tag{19}$$

$$E_P = \int_{\delta_a}^{\delta_b} P_m - V_g \sin\delta \mathrm{d}\delta \tag{20}$$

If there exists a critical E_D such that the system power angle operates at δ_b with $\Delta\omega_b = 0$, this corresponds to the minimum damping dissipation energy $E_{D\min}$. If Formula (21) is satisfied, the kinetic energy of the system will be dissipated, and then the power angle will ultimately stabilize at the stable equilibrium point of the n-th cycle

$$E_P < E_{D\min} < E_D \tag{21}$$

The proof process is as follows.

Assuming that the fault is cleared within the k-th cycle, Formula (22) can be derived:

$$E_{P(k,k+1)} < E_{D(k,k+1)} \tag{22}$$

In Formula (22), $E_{P(k,k+1)}$ and $E_{D(k,k+1)}$ represent the variation in potential energy and the energy dissipated by damping of the power angle from the k-th stable equilibrium point to the $(k+1)$-th stable equilibrium point, respectively. Formula (23) can be derived based on the energy transformation relations as follows:

$$E_{K(k+1)} - E_{K(k)} = E_{P(k,k+1)} - E_{D(k,k+1)} < 0 \Rightarrow E_{K(k+1)} < E_{K(k)} \tag{23}$$

In Formula (23), $E_{K(k)}$ represents the kinetic energy of the power angle at the k-th stable equilibrium point. It can be seen from Formula (23) that after fault clearance, if Formula (24) holds, the kinetic energy of the system will decrease with each power angle cycle, which can be expressed as Formula (24):

$$0 < E_{K(n)} < \cdots < E_{K(k+1)} < E_{K(k)} < \cdots < E_1 \tag{24}$$

Specifically, if Formula (25) holds, then Formula (26) is valid. However, it can be seen from Formula (9) that $E_{K(n+1)} \geq 0$, which contradicts Formula (26). Therefore, $E_{K(n+1)}$ does not exist, indicating that the power angle ultimately stabilizes at the stable equilibrium point of the n-th cycle.

$$E_{K(n)} < E_{D(n,n+1)} - E_{P(n,n+1)} \tag{25}$$

$$0 - E_{K(n)} < E_{P(n,n+1)} - E_{D(n,n+1)} = E_{K(n+1)} - E_{K(n)} \Rightarrow E_{K(n+1)} < 0 \tag{26}$$

Based on the above analysis, it can be concluded that, if the variation in potential energy within one power angle cycle is lower than the minimum damping dissipation energy, the kinetic energy will gradually decrease, and eventually, the system will recover stability.

The equal energy trajectories of the system are shown in Figure 8, where all points on the same energy trajectory have equal energy. C_{min} is the critical energy trajectory in the upper half-plane, and C_{eq} represents the energy trajectory passing through (δ_b, 0) when damping is ignored, with the corresponding damping dissipation energy being zero. According to Figure 8, the energy of trajectory C_{eq} can be expressed as

$$V(\delta_b, 0) = -P_m\delta_b - V_g \cos\delta_b + E_0 \tag{27}$$

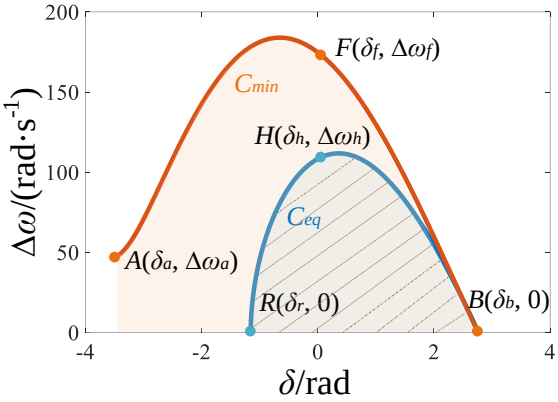


Figure 8. Equal energy trajectory.

Assume that $F(\delta_f, \Delta\omega_f)$ and $H(\delta_h, \Delta\omega_h)$ are arbitrary points on C_{eq} and C_{min}, respectively. When $\delta_f \in [\delta_a, \delta_r)$, Ceq does not exist in this interval. When $\delta_f \in [\delta_r, \delta_b)$, let $\delta_f = \delta_h$. According to Formula (8), we have

$$V\left(\delta_f, \dot{\delta}_f\right) - V\left(\delta_h, \dot{\delta}_h\right) = V\left(\delta_f, \dot{\delta}_f\right) - V(\delta_b, 0) = D_{eq}\int_{\delta_f}^{\delta_b} \dot{\delta}\mathrm{d}\delta > 0 \tag{28}$$

$$V\left(\delta_f, \dot{\delta}_f\right) > V\left(\delta_h, \dot{\delta}_h\right) \Rightarrow \dot{\delta}_f > \dot{\delta}_h \tag{29}$$

It can be seen from Formula (29) that f always lies above h. Therefore, in the upper half-plane, the equal energy trajectory C_{eq} always remains below the critical curve C_{min}.

To avoid reliance on information during a fault, the maximum acceleration area is selected to design a conservative damping coefficient. From Figure 9, it can be found that the conditions of maximum acceleration area have two parts: the first is that the voltage is decreased to zero; the second is that the fault clearing time is at $\delta = (2i-1)\pi$ in the ith swinging period. It has a fixed deceleration area in the next swinging period, which can offset some of the acceleration energy. Therefore, according to the equal-area criterion, the residue acceleration energy can be expressed as

$$E_P = \int_{\delta_{s,i}}^{\delta_{r,i}} P_m\mathrm{d}\delta - \int_{(2i-1)\pi}^{\delta_{r,i}} V_g \sin\delta\mathrm{d}\delta = P_m(\delta_{r,i} - \delta_{s,i}) + V_g(\cos\delta_{r,i} + 1) \tag{30}$$

and the $\delta_{r,i}$ can be calculated as follows:

$$\int_{\delta_{r,i}}^{\delta_{u,i+1}} \left(P_m - V_g \sin\delta\right)\mathrm{d}\delta = 0 \tag{31}$$

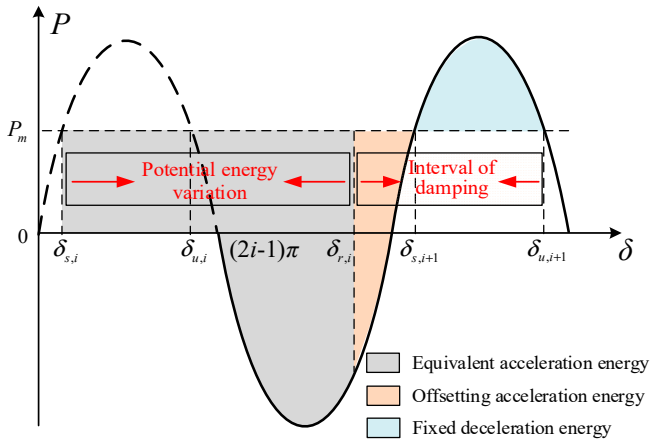


Figure 9. Design principle of damping feedback coefficient.

If the variation in potential energy during the movement of the power angle from $\delta_{s,i}$ to $\delta_{r,i}$ does not exceed the energy dissipated by damping from $\delta_{r,i}$ to $\delta_{u,i+1}$, then after fault clearance, the deceleration energy of the system in any cycle will always be greater than the acceleration energy. Therefore, the kinetic energy will gradually decrease, and the power angle will ultimately recover stability. Let S_{Ceq} denote the area enclosed by the equal energy trajectory C_{eq}, which can be expressed as Formula (32). Thus, the dissipation energy caused by damping can be conservatively expressed as

$$S_{Ceq} = \int_{\delta_{r,i}}^{\delta_{u,i+1}} \sqrt{\int_{\delta_{r,i}}^{\delta} \frac{2}{J}(P_m - V_g \sin\delta)\mathrm{d}\delta\mathrm{d}\delta} \tag{32}$$

$$E_D = D_{eq} S_{Ceq} \tag{33}$$

From Formula (21), it is known that $E_D \geq E_P$. Therefore, the switching value of the damping feedback coefficient at the fault occurrence time can be expressed as

$$D_f \geq \frac{P_m(\delta_{r,i} - \delta_{s,i}) + V_g(\cos\delta_{r,i} + 1)}{\sqrt{\frac{2}{J}}\int_{\delta_{r.i}}^{\delta_{u,i+1}} \sqrt{P_m(\delta - \delta_{r,i}) + V_g(\cos\delta - \cos\delta_{r,i})}\mathrm{d}\delta} + L_g I_{dref} \tag{34}$$

4.2. Practical Processing of IPLL Parameter Design

From Formula (34), the damping design of IPLL is related to grid parameters and operating parameters, which poses challenges for engineering applications. Therefore, conservative treatment is applied to the above parameters, so that the design of the IPLL damping feedback coefficient is solely determined by the rated parameters and the given SCR.

From Formula (6), if the feedback gain D satisfies Formula (35) under any conditions, the equivalent damping coefficient can always be positive:

$$D > \max\left|L_g I_{dref}\right| \tag{35}$$

Also, Formula (35) can be rewritten as follows:

$$\omega_0 D > \max\left|\omega_0 L_g I_{dref}\right| = \max\left|\omega_0 L_g\right|\left|I_{dref}\right| \tag{36}$$

According to the vector relationships shown in Figure 10, it can be seen that $|\omega_{0Lg}| \leq |Z_g|$, $|I_{dref}| \leq |I_{ref}|$. Here, I_{ref} is the rated current of the inverter. Therefore, Formula (36) can be rewritten as follows:

$$\omega_0 D > \max\left|\mathbf{Z}_g\right|\left|\mathbf{I}_{ref}\right| \tag{37}$$

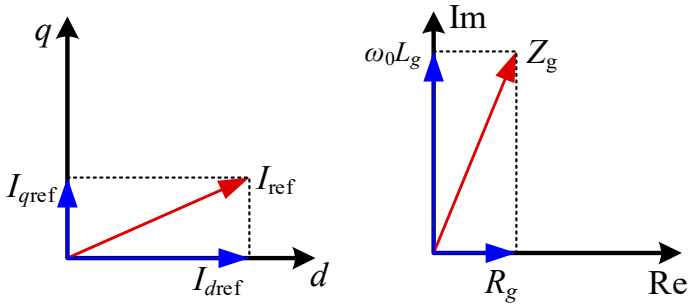


Figure 10. Vector relationship diagrams.

Suppose that the rated capacity P_N of the inverter and the short-circuit capacity P_{sc} of grid are expressed in Formulas (38) and (39):

$$P_N = \left|\mathbf{V}_{ref}\right|\left|\mathbf{I}_{ref}\right| \tag{38}$$

$$P_{sc} = \frac{\left|\mathbf{V}_{ref}\right|^2}{\left|\mathbf{Z}_g\right|} \tag{39}$$

Therefore, the short-circuit capacity ratio (SCR) of the system can be obtained using Formula (40):

$$\mathrm{SCR} = \frac{P_{sc}}{P_N} = \frac{\left|\mathbf{V}_{ref}\right|}{\left|\mathbf{Z}_g\right|\left|\mathbf{I}_{ref}\right|} \tag{40}$$

Under the worst condition, SCR = 1; therefore, the damping coefficient D can be designed using Formula (41):

$$D > \frac{\left|\mathbf{V}_{ref}\right|}{\omega_0} = \frac{V_{ref}}{\omega_0} \tag{41}$$

Considering the fluctuation of grid voltage and frequency, a conservative design of feedback gain is $D = (k_1 V_{ref})/(k_2 \omega_0)$. Here, k_1 and k_2 are the voltage and frequency fluctuation coefficients. Therefore, a constantly positive damping coefficient of IPLL is guaranteed under different grid conditions.

Since the reactance is much larger than the resistance in high-voltage transmission lines, $X_g \approx |\mathbf{Z}_g|$. Under rated operating conditions, $I_{dref} = |\mathbf{I}_{ref}|$ and $I_{qref} = 0$. Thus, we have

$$L_g I_{dref} \approx \frac{\left|\mathbf{Z}_g\right|\left|\mathbf{I}_{ref}\right|}{\omega_0} = \frac{V_{ref}}{\omega_0 \mathrm{SCR}} \tag{42}$$

Thus, the equivalent mechanical power P_m can be expressed as Formula (43):

$$P_m = \omega_0 L_g I_{dref} = \frac{V_{ref}}{\mathrm{SCR}} \tag{43}$$

When the system is under normal operating conditions, Formula (44) holds:

$$\begin{cases} \delta_{s,i} = \arcsin\frac{P_m}{V_g} = \arcsin\frac{1}{\mathrm{SCR}} + 2(i-1)\pi \\ \delta_{u,i} = (2i-1)\pi - \delta_{s,i} \end{cases} \tag{44}$$

By substituting Formulas (42)–(44) into Formula (31) and (34), the design of the damping feedback coefficient is determined solely by the SCR and rated parameters.

The equal energy trajectories of the system under different SCRs ($J = 0.05$, $D = 2$) are shown in Figure 11. As the SCR decreases, the contraction of the equal energy trajectory

is observed, with the area enclosed by the abscissa reduced, and the damping coefficient tuned by the design method is increased. Particularly, when SCR = 1, the equal energy trajectory in Figure 10 is contracted to the point ($\pi/2$, 0), with the area enclosed by the abscissa being zero, and the theoretically required damping coefficient is infinite. Since SCR = 1 is impossible in actual grid, a certain conservativeness is taken into account, and SCR is set to 1.1 in the parameter design of IPLL, thereby ensuring the effectiveness of the proposed method under grid conditions with SCR $\geq$ 1.1.

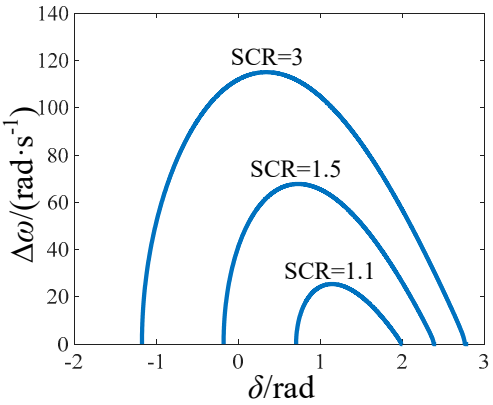


Figure 11. Equal energy trajectories of the system under different SCRs (J = 0.05, D = 2).

The damping coefficient switching control flow is shown in Figure 12. First, corresponding operations are performed based on whether a short-circuit fault occurs in the system. D is set to D_n when the system is in normal operation and is switched to D_f when a short-circuit fault is detected. After the fault is cleared and the frequency recovers to stability, D is switched back to D_n.

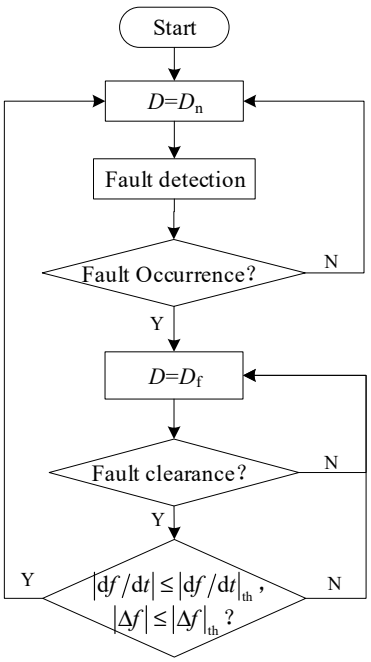


Figure 12. Damping coefficient switching control flow.

5. Experimental Verification

5.1. Setup of HIL Platform

To validate the theoretical analysis results in previous sections, a hardware-in-loop (HIL) platform of the grid-connected inverter system is established, as shown in Figure 13.

The hardware of the three-phase inverter is configured in the StarSim HIL5.3.0 host computer software and runs on the MT6020 real-time simulator with a time step of 1 μs. The control algorithm is implemented in the TMS320C28346 digital signal processing controller (DSP), and the sampling frequency is 10 kHz. A Xilinx XC6SLX16 field programmable gate array (FPGA) is adopted to achieve the modulation scheme and generate gate signals of all IGBTs. The analog/digital signal interaction between the controller and the real-time simulator is realized using an I/O board. Also, the oscilloscope captures the analog output signals to show the experimental results. The parameters of this system are listed in Table 2.

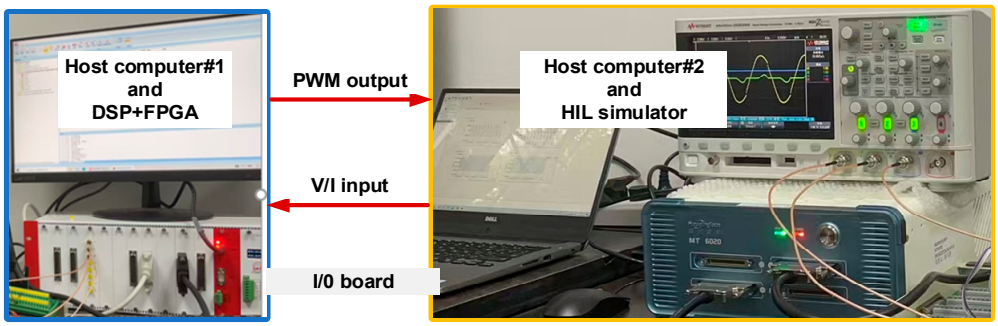


Figure 13. HIL experimental platform.

Table 2. Parameters of system.

Parameter	Value
DC voltage V_{dc}	700 V
Grid voltage V_g	311 V
Rated frequency f_n	50 Hz
Rated current I_n	80 A
Active current reference I_{dref}	80 A
Reactive current reference I_{qref}	0
Filter inductance L_f	3.5 mH
Line inductance L_g	4.1 mH
Inertia coefficient J of IPLL	0.05
Damping feedback coefficient D_n of IPLL	2
Proportional coefficient K_p of PLL	0.1305
Integral coefficient K_i of PLL	19.144
Proportional coefficient K_{pc} of current loop PI control	27.49
Integral coefficient K_{ic} of current loop PI control	785.40

5.2. Accurate Phase-Locked Capability of IPLL-Synchronized Inverter

Due to the real-time variation in the grid frequency, it is necessary to verify whether the proposed IPLL-synchronized inverter can accurately lock the phase under different grid frequencies. Therefore, three cases with different grid frequencies are set. Corresponding experimental waveforms are shown in Figure 14. It can be seen that the q-axis voltage transferred by θ_{real} is always zero under different grid frequencies, which means that the IPLL can catch the right phase of PCC's voltage. Also, the partial enlarged images also show that the A-phase voltage and A-phase current operate in phase. As a result, the proposed IPLL can accurately lock the phase under different grid frequencies.

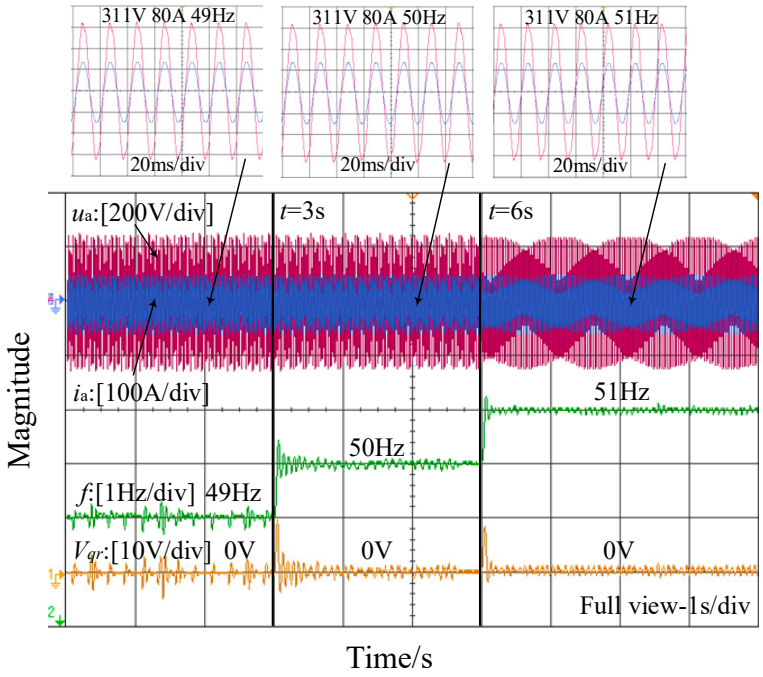


Figure 14. Experimental waveforms of IPLL at different grid frequencies.

5.3. Comparison of Transient Stability Between PLL-Synchronized Inverter and IPLL-Synchronized Inverter

From Figure 8, it can be seen that the stability region of the IPLL-synchronized inverter is larger than that of the PLL-synchronized inverter. In order to verify its correctness, the grid voltage sags to 0.2 pu at t = 3 s, and this fault is cleared at t = 3.06 s. The corresponding phase trajectories are shown in Figure 15. From Figure 15, since the equivalent damping coefficient of the PLL-synchronized inverter is related to the power angle, the equivalent damping coefficient gradually decreases until it becomes negative. Compared with the IPLL-synchronized inverter, under the same fault duration, the phase trajectory exceeds the boundary of the stability region. As for the IPLL-synchronized inverter, since the damping is always positive, the phase trajectory change is slow. Further, its stability region is larger than that of the PLL-synchronized inverter, and the IPLL-synchronized inverter achieves transient stability.

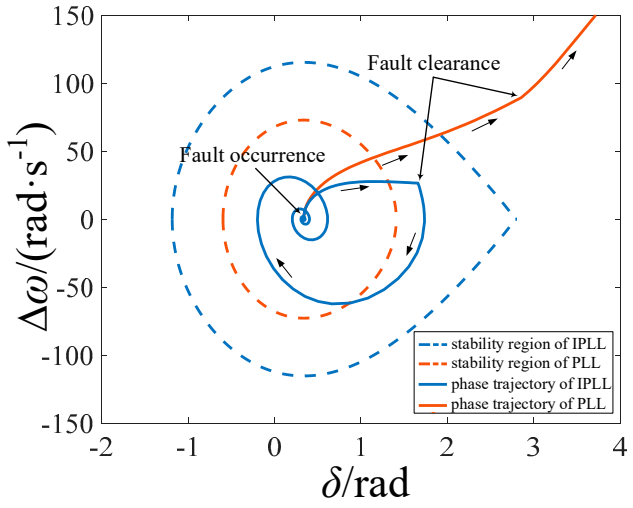


Figure 15. Phase trajectories at Δt = 0.06 s.

Corresponding experimental waveforms are shown in Figure 16. Under the same fault, the IPLL-synchronized inverter can restore stable operation, but the PLL-synchronized inverter loses transient stability.

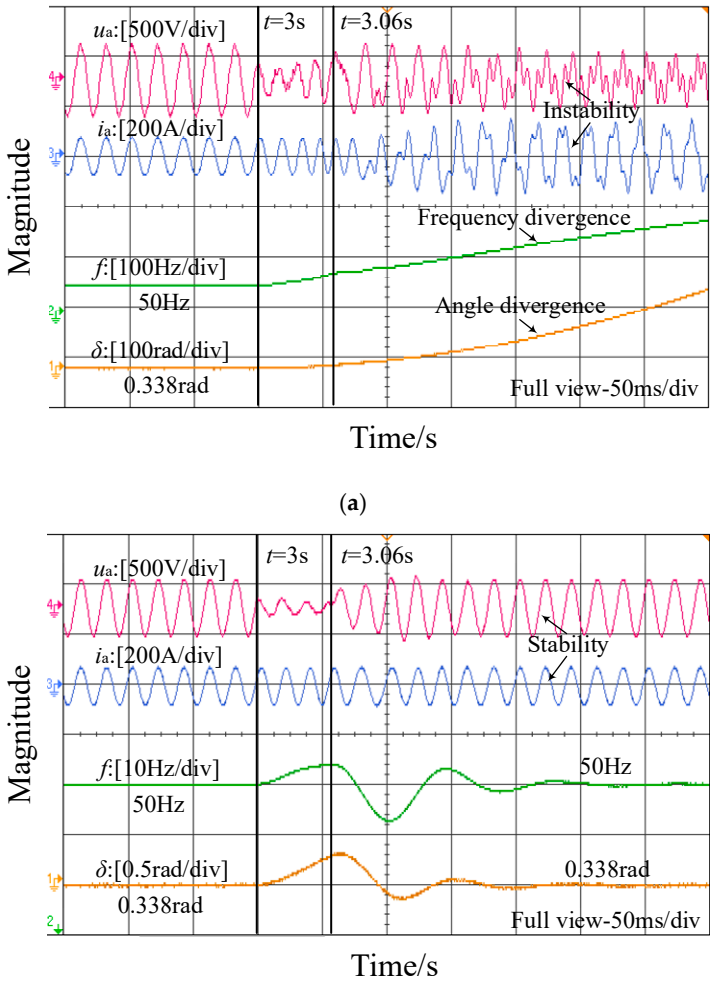


Figure 16. Experimental waveforms at Δt = 0.06 s. (**a**) PLL; (**b**) IPLL.

5.4. Verification of the Proposed Damping Switching Control Strategy Under Different Conditions

To verify the effectiveness of the proposed damping switching control strategy, some cases and their experimental results are listed in Table 3. Based on the parameters in Table 1, the required switching value of the damping feedback coefficient at the fault occurrence moment can be calculated as D_f = 96.67.

(1) Under Different Voltage Sags: Cases 1~3 are used to verify its effectiveness under different voltage sags. The corresponding phase trajectories are shown in Figure 17. When the grid voltage sags to 0.6 and 0.4 pu, the fault severity is mild, and the system maintains a stable balance point, such that the IPLL remains stable during and after fault clearance. When the grid voltage sags to 0.2 pu, the stable equilibrium point is absent, causing the power angle to increase continuously. Substantial decelerating energy is supplied during the fault due to the IPLL providing sufficient positive damping, slowing down the rate of power angle increase. The power angle does not cross the first-cycle unstable equilibrium point after fault clearance, thus recovering to the original stable equilibrium point $\delta_{s,1}$ = 0.3377 rad.

Table 3. Study cases.

No	Cases	V_g/V	L_g/mH	Δt/s	Restore Stability	Theoretical Stable Equilibrium Point	Experimental Stable Equilibrium Point
1	Basic case	62 (0.2 pu)	4.1 (SCR = 3)	3	Yes	$\delta_{s,1}$ = 0.3377 rad	$\delta_{s,1}$ = 0.338 rad
2	Different voltage sags	124 (0.4 pu)	4.1 (SCR = 3)	3	Yes	$\delta_{s,1}$ = 0.3377 rad	$\delta_{s,1}$ = 0.338 rad
3		187 (0.6 pu)	4.1 (SCR = 3)	3	Yes	$\delta_{s,1}$ = 0.3377 rad	$\delta_{s,1}$ = 0.338 rad
4	Longer fault duration	62 (0.2 pu)	4.1 (SCR = 3)	5	Yes	$\delta_{s,2}$ = 6.6209 rad	$\delta_{s,2}$ = 6.621 rad
5	Extremely weak grid	62 (0.2 pu)	8.2 (SCR = 1.5)	2	Yes	$\delta_{s,2}$ = 7.0076 rad	$\delta_{s,2}$ = 7.008 rad

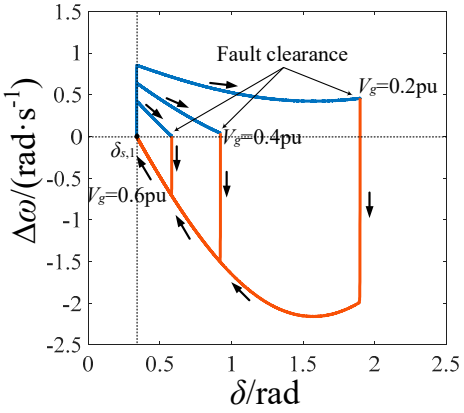


Figure 17. Phase trajectories under different grid voltage sags.

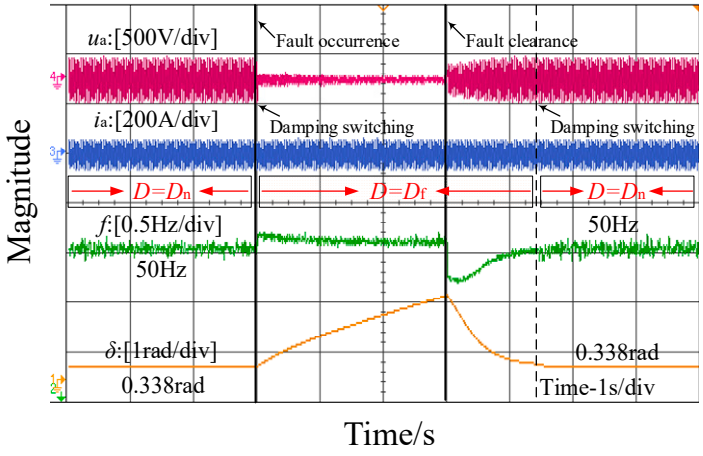
The experimental waveforms of IPLL when the grid voltage sags to 0.2 pu are shown in Figure 18. The positive damping of IPLL provides sufficient decelerating energy, enabling the power angle to recover to the original stable equilibrium point $\delta_{s,1}$ = 0.338 rad after fault clearance.

(2) Longer Fault Duration: Cases 1 and 4 are used to verify the effectiveness of the proposed method under longer fault durations, and the corresponding phase trajectories are shown in Figure 19. The power angle recovers to the original stable equilibrium point $\delta_{s,2}$ = 0.3377 rad after fault clearance when the fault duration is 3 s. When the fault duration is 5 s, the power angle crosses the first-cycle unstable equilibrium point. Due to the sufficient decelerating energy provided by the constant positive damping, the power angle can stabilize at the stable equilibrium point $\delta_{s,2}$ = 6.6209 rad within the second cycle after fault clearance.

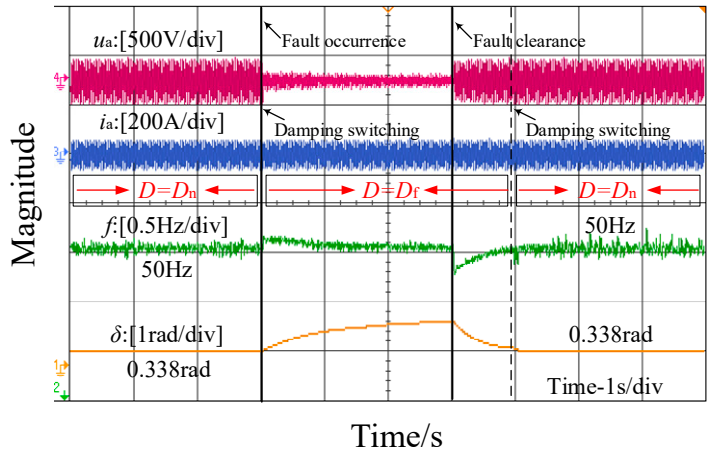
The experimental waveforms of IPLL when the grid voltage sags to 0.2 pu with a fault duration of 5 s are shown in Figure 20. The system frequency fluctuates within a small range during the fault, and the power angle stabilizes at $\delta_{s,2}$ = 6.621 rad after fault clearance, which verifies the correctness of the phase portrait analysis.

(3) Extremely weak grid: Case 5 is used to verify the effectiveness of the proposed method under extremely weak-grid conditions (SCR = 1.5). The corresponding phase trajectories are shown in Figure 21. When L_g = 8.2 mH (SCR = 1.5), the power angle of the system stabilizes at $\delta_{s,1}$ = 0.7244 rad. Similarly to previous cases, the power angle of IPLL increases during the fault, crosses the unstable equilibrium point, and enters the second cycle. Due to the effect of positive damping, kinetic energy is not accumulated, and the frequency remains within a certain range. After fault

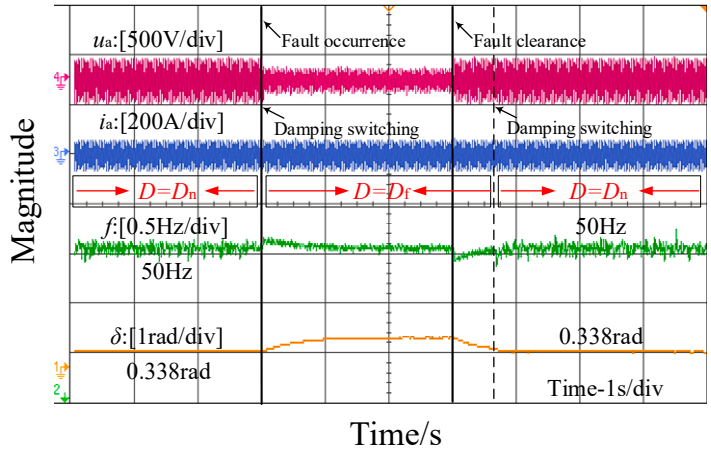
clearance, the power angle stabilizes at the stable equilibrium point of the second cycle, $\delta_{s,2}$ = 7.0076 rad.



(**a**)



(**b**)



(**c**)

Figure 18. Experimental waveforms under different grid voltage sags. (**a**) 0.2 pu; (**b**) 0.4 pu; (**c**) 0.6 pu.

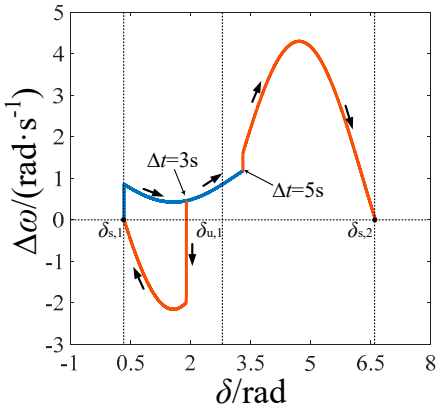


Figure 19. Phase trajectories at different fault durations.

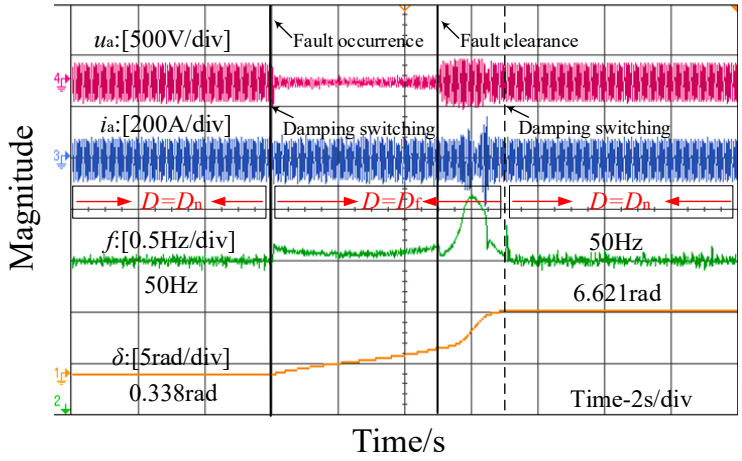


Figure 20. Experimental waveforms at Δt = 5 s.

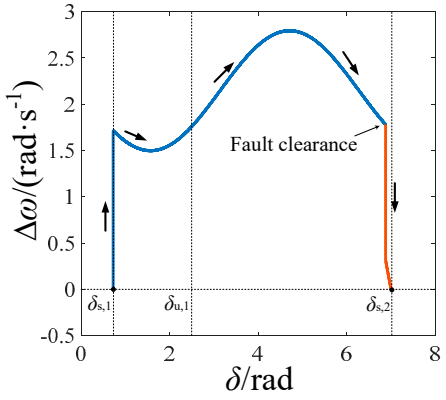


Figure 21. Phase trajectories under extremely weak-grid conditions (SCR = 1.5).

The experimental waveforms shown in Figure 22 indicate no kinetic energy accumulation during the fault, and the power angle stabilizes at the new stable equilibrium point $\delta_{s,2}$ = 7.008 rad after fault clearance, which verifies the effectiveness of the proposed IPLL and the damping switching control strategy under extremely weak-grid conditions.

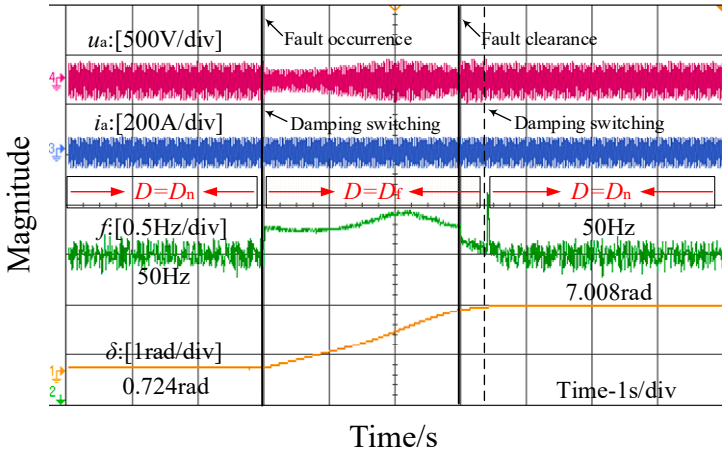


Figure 22. Experimental waveforms under extremely weak-grid conditions (SCR = 1.5).

6. Conclusions

To address the issue of transient instability caused by indefinite damping in a traditional PLL-synchronized inverter, this paper proposes an improved PLL structure. On this basis, a damping coefficient switching control considering transient stability improvement is proposed. The main conclusions are as follows:

(1) By removing the proportional branch of the traditional PLL and adding a positive damping feedback branch, the IPLL fundamentally eliminates the nonlinear coupling between the equivalent damping coefficient and the power angle. Theoretical analysis and HIL experiments confirm that the equivalent damping of the IPLL-synchronized system remains positive across all operating conditions, resolving the inherent indefinite damping issue of traditional PLLs. Compared to traditional PLL, the IPLL expands the system's stable region, significantly enhancing transient stability margins.

(2) The proposed damping coefficient switching strategy leverages positive damping to dissipate transient energy. During faults, switching to a pre-calculated high damping coefficient rapidly suppresses power angle oscillations. Post-fault, reverting to the nominal damping coefficient ensures steady-state performance. Experiments under various conditions (voltage sags of 0.2–0.6 pu, fault durations of 3–5 s, and SCR = 1.5) demonstrate that the strategy prevents kinetic energy accumulation, enabling the system to stabilize at equilibrium points.

(3) The damping coefficient is designed offline using rated parameters and SCRs, avoiding reliance on real-time grid parameter estimation. This feature makes the strategy adaptable to diverse grid conditions, including weak and ultra-weak grids. The experimental results validate its effectiveness in fault recovery under extreme scenarios, providing a practical and reliable solution for transient stability control in high-penetration new energy grid-connected systems.

Author Contributions: Conceptualization, K.J.; methodology, K.J.; software, K.J.; validation, D.L.; formal analysis, D.L.; investigation, K.J.; resources, D.L.; data curation, D.L.; writing—original draft preparation, K.J.; writing—review and editing, K.J. and D.L.; visualization, D.L.; supervision, K.J. and D.L.; project administration, D.L.; funding acquisition, K.J. All authors have read and agreed to the published version of the manuscript.

Funding: This research was funded by the science and technology project of State Grid Hubei Electric Power Co., Ltd., grant number 52153224002L.

Data Availability Statement: Data are within the article.

Acknowledgments: We acknowledge the support of colleagues and the science and technology project of state grid corporation of China.

Conflicts of Interest: Kezheng Jiang and Dan Liu were employed by State Grid Hubei Electric Power Research Institute. The remaining authors declare that the research was conducted in the absence of any commercial or financial relationships that could be construed as a potential conflict of interest. The authors declare that this study received funding from State Grid Hubei Electric Power Co., Ltd. The funder was not involved in the study design, collection, analysis, interpretation of data, the writing of this article or the decision to submit it for publication.

References

1. Tian, X.; Zhang, Y.; Xu, Y.; Zheng, L.; Zhang, L.; Yuan, Z. Transient Synchronous Stability Modeling and Comparative Analysis of Grid-Following and Grid-Forming New Energy Power Sources. *Electronics* **2024**, *13*, 3308. [CrossRef]
2. Pei, J.; Yao, J.; Liu, R.; Zeng, D.; Sun, P.; Zhang, H.; Liu, Y. Characteristic Analysis and Risk Assessment for Voltage–Frequency Coupled Transient Instability of Large-Scale Grid-Connected Renewable Energy Plants During LVRT. *IEEE Trans. Ind. Electron.* **2020**, *67*, 5515–5530. [CrossRef]
3. He, X.; Geng, H.; Xi, J.; Guerrero, J.M. Resynchronization Analysis and Improvement of Grid-Connected VSCs During Grid Faults. *IEEE J. Emerg. Sel. Top. Power Electron.* **2021**, *9*, 438–450. [CrossRef]
4. Fu, X.; Sun, J.; Huang, M.; Tian, Z.; Yan, H.; Iu, H.H.-C.; Hu, P.; Zha, X. Large-Signal Stability of Grid-Forming and Grid-Following Controls in Voltage Source Converter: A Comparative Study. *IEEE Trans. Power Electron.* **2021**, *36*, 7832–7840. [CrossRef]
5. Mansour, M.Z.; Me, S.P.; Hadavi, S.; Badrzadeh, B.; Karimi, A.; Bahrani, B. Nonlinear Transient Stability Analysis of Phased-Locked Loop-Based Grid-Following Voltage-Source Converters Using Lyapunov's Direct Method. *IEEE J. Emerg. Sel. Top. Power Electron.* **2022**, *10*, 2699–2709. [CrossRef]
6. Zhao, J.; Huang, M.; Zha, X. Nonlinear Analysis of PLL Damping Characteristics in Weak-Grid-Tied Inverters. *IEEE Trans. Circuits Syst. II Express Briefs* **2020**, *67*, 2752–2756. [CrossRef]
7. Zhao, J.; Huang, M.; Yan, H.; Tse, C.K.; Zha, X. Nonlinear and Transient Stability Analysis of Phase-Locked Loops in Grid-Connected Converters. *IEEE Trans. Power Electron.* **2021**, *36*, 1018–1029. [CrossRef]
8. Zhang, Y.; Zhang, C.; Cai, X. Large-Signal Grid-Synchronization Stability Analysis of PLL-Based VSCs Using Lyapunov's Direct Method. *IEEE Trans. Power Syst.* **2022**, *37*, 788–791. [CrossRef]
9. Taul, M.G.; Wang, X.; Davari, P.; Blaabjerg, F. An Overview of Assessment Methods for Synchronization Stability of Grid-Connected Converters Under Severe Symmetrical Grid Faults. *IEEE Trans. Power Electron.* **2019**, *34*, 9655–9670. [CrossRef]
10. Tang, Y.; Tian, Z.; Zha, X.; Li, X.; Huang, M.; Sun, J. An Improved Equal Area Criterion for Transient Stability Analysis of Converter-Based Microgrid Considering Nonlinear Damping Effect. *IEEE Trans. Power Electron.* **2022**, *37*, 11272–11284. [CrossRef]
11. Li, X.; Tian, Z.; Zha, X.; Sun, P.; Hu, Y.; Huang, M. An Iterative Equal Area Criterion for Transient Stability Analysis of Grid-Tied Converter Systems with Varying Damping. *IEEE Trans. Power Syst.* **2024**, *39*, 1771–1784. [CrossRef]
12. Ma, S.; Geng, H.; Liu, L.; Yang, G.; Pal, B.C. Grid-Synchronization Stability Improvement of Large Scale Wind Farm During Severe Grid Fault. *IEEE Trans. Power Syst.* **2018**, *33*, 216–226. [CrossRef]
13. Wang, X.; Wu, H.; Wang, X.; Dall, L.; Kwon, J.B. Transient Stability Analysis of Grid-Following VSCs Considering Voltage-Dependent Current Injection During Fault Ride-Through. *IEEE Trans. Energy Convers.* **2022**, *37*, 2749–2760. [CrossRef]
14. Xu, D.; Zhan, M. Transient Stability Analysis and Enhancement of PLL-VSC Considering State-Dependent Damping. *IEEE Access* **2023**, *11*, 137485–137494. [CrossRef]
15. Liu, Y.; Yao, J.; Pei, J.; Zhao, Y.; Sun, P.; Zeng, D.; Chen, S. Transient Stability Enhancement Control Strategy Based on Improved PLL for Grid Connected VSC during Severe Grid Fault. *IEEE Trans. Energy Convers.* **2021**, *36*, 218–229. [CrossRef]
16. Wu, C.; Xiong, X.; Taul, M.G.; Blaabjerg, F. Enhancing Transient Stability of PLL-Synchronized Converters by Introducing Voltage Normalization Control. *IEEE J. Emerg. Sel. Top. Circuits Syst.* **2021**, *11*, 69–78. [CrossRef]
17. Zhang, C.; Chen, J.; Si, W. Analysis of Phase-Locked Loop Filter Delay on Transient Stability of Grid-Following Converters. *Electronics* **2024**, *13*, 986. [CrossRef]
18. Chen, Z.; Guan, L. Transient Synchronous Stability Analysis and Control Improvement for Power Systems with Grid-Following Converters. *Electronics* **2025**, *14*, 3263. [CrossRef]
19. Taul, M.G.; Wang, X.; Davari, P.; Blaabjerg, F. Robust Fault Ride Through of Converter-Based Generation During Severe Faults With Phase Jumps. *IEEE Trans. Ind. Appl.* **2020**, *56*, 570–583. [CrossRef]
20. Wu, H.; Wang, X. Design-Oriented Transient Stability Analysis of PLL-Synchronized Voltage-Source Converters. *IEEE Trans. Power Electron.* **2020**, *35*, 3573–3589. [CrossRef]
21. Tang, Y.; Li, Y. Common Lyapunov Function Based Stability Analysis of VSC With Limits of Phase Locked Loop. *IEEE Trans. Power Syst.* **2023**, *38*, 1759–1762. [CrossRef]

22. Fu, X.; Huang, M.; Tse, C.K.; Yang, J.; Ling, Y.; Zha, X. Synchronization Stability of Grid-Following VSC Considering Interactions of Inner Current Loop and Parallel-Connected Converters. *IEEE Trans. Smart Grid* **2023**, *14*, 4230–4241. [CrossRef]
23. Nagam, S.S.; Pal, B.C.; Wu, H.; Blaabjerg, F. Synchronization Stability Analysis of SRF-PLL and DSOGI-PLL Using Port-Hamiltonian Framework. *IEEE Trans. Control Syst. Technol.* **2025**, *33*, 952–962. [CrossRef]
24. Li, Y.; Lu, Y.; Tang, Y.; Du, Z. Conditions of Existence and Uniqueness of Limit Cycle for Grid-Connected VSC with PLL. *IEEE Trans. Power Syst.* **2024**, *39*, 706–719. [CrossRef]

Disclaimer/Publisher's Note: The statements, opinions and data contained in all publications are solely those of the individual author(s) and contributor(s) and not of MDPI and/or the editor(s). MDPI and/or the editor(s) disclaim responsibility for any injury to people or property resulting from any ideas, methods, instructions or products referred to in the content.